Environmental Science & Technology

Article

pubs.acs.org/est

Roles of Transport Limitations and Mineral Heterogeneity in Carbonation of Fractured Basalts

Anne H. Menefee,[†] Peiyuan Li,[†] Daniel E. Giammar,[‡] and Brian R. Ellis*[,†]

[†]Department of Civil and Environmental Engineering, University of Michigan, Ann Arbor, Michigan 48109, United States

[‡]Department of Energy, Environmental, and Chemical Engineering, Washington University, St. Louis, Missouri 63130, United States

Supporting Information

ABSTRACT: Basalt formations could enable secure long-term carbon storage by trapping injected CO_2 as stable carbonates. Here, a predictive modeling framework was designed to evaluate the roles of transport limitations and mineral spatial distributions on mineral dissolution and carbonation reactions in fractured basalts exposed to CO_2-acidified fluids. Reactive transport models were developed in CrunchTope based on data from high-temperature, high-pressure flow-through experiments. Models isolating the effect of transport compared nine flow conditions under the same mineralogy. Heterogeneities were incorporated by segmenting an actual reacted basalt sample, and these results were compared to equivalent flow conditions through randomly generated mineral distributions with the same bulk composition. While pure advective flow with shorter retention times promotes rapid initial carbonation, pure diffusion sustains mineral reactions for longer time frames and generates greater net carbonate volumes. For the same transport conditions and bulk composition, exact mineral spatial distributions do not impact the amount of carbonation but could determine the location by controlling local solution saturation with respect to secondary carbonates. In combination, the results indicate that bulk mineralogy will be more significant than small-scale heterogeneities in controlling the rate and extent of CO_2 mineralization, which will likely occur in diffusive zones adjacent to flow paths or in dead-end fractures.

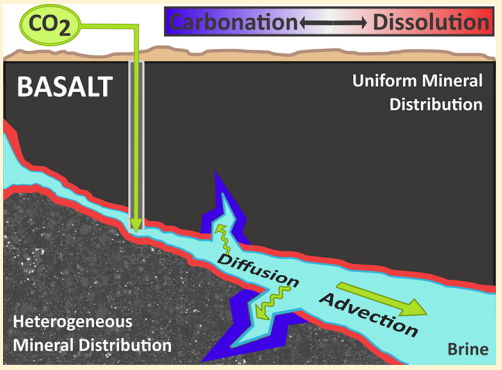

1. INTRODUCTION

The drive to mitigate anthropogenic CO_2 emissions associated with rising energy demands has motivated research efforts on an array of carbon capture, utilization, and storage strategies. Research in geologic carbon storage has centered on ubiquitous and well-characterized sedimentary formations that primarily rely on physical containment of injected CO_2. Associated leakage risks (e.g., through breached caprocks or abandoned wells)[1] have prompted interest in utilizing alternative reservoirs with higher abundances of reactive minerals that could provide secure long-term carbon trapping.[2] Flood basalts are particularly attractive, as rapid mineral dissolution promoted by CO_2 injection releases divalent metal cations that can then combine with CO_2 to form stable carbonates.[3] Despite investigations at both lab[4,5] and pilot[6,7] scales, our understanding of the fundamental controls on this process along with its viability as a permanent sequestration option remain limited.

Because transport limitations likely dictate both the speed and extent of mineral carbonation, characterizing basalt alterations resulting from CO_2 injection under different flow regimes is crucial to predicting microstructural changes that impact sustained CO_2 injection and trapping rates. Through a series of reactive percolation experiments in sintered magmatic olivine cores, Peuble et al.[8] concluded that higher flow rates result in greater carbonation efficiency because permeability reductions can block transport in low-flow regions. In addition, they confirmed that secondary precipitates controlled by rock dissolution occurred in diffusion-dominated paths, while those limited by influent fluid composition formed along advective paths. Andreani et al.[9] also conducted percolation experiments on sintered dunite and only observed significant carbonate-induced porosity alterations in dead-end zones, whereas high-flow zones promoted rapid dissolution followed by the formation of a passivating Si-rich surface layer that created a barrier between fluids and reactive surfaces. Such studies highlight the need to optimize injection strategies that promote primary mineral dissolution while maintaining adequate conditions for mineral carbonation.

The effects of mineral spatial distributions on the extent of CO_2 mineralization in basalts are less established but are likely coupled with the effects of transport limitations. Peuble et al.[8] noted that carbonation rates were a function of complex interactions between flow conditions, kinetics, and mineral heterogeneities. Due to these complexities, secondary carbonate precipitation was localized and subsequently inhibited flow. Conversely, Andreani et al.[9] observed that localized precipitation along preferential flow paths resulting from mineral

Received: January 19, 2017
Revised: April 25, 2017
Accepted: July 12, 2017
Published: July 12, 2017

DOI: 10.1021/acs.est.7b00326
Environ. Sci. Technol. 2017, 51, 9352−9362

heterogeneities generated simultaneous increases in permeability and rock volume that would support continued CO_2 trapping. Xiong and Giammar[10] attributed localized carbonate formation in packed forsterite beds to geochemical gradients induced by diffusion-limited transport, while Giammar et al.[11] showed that magnesite can form in diffusive regions before volume-averaged properties reach saturation. Several studies have also demonstrated the influence of heterogeneities on mineral dissolution, an anticipated rate-limiting factor for mineral carbonation. Salehikhoo et al.[12] found that magnesite dissolution rates varied by no more than 14% under different spatial distributions of magnesite within quartz samples, but that variations in rates due to heterogeneities were most pronounced under mixed flow conditions compared with advection- and diffusion-limiting regimes. Li et al.[13] extended this work, confirming modeling indications that random mineral distributions with smaller clustering result in greater dissolution than distributions with larger discrete mineral zones. Similarly, Molins et al.[14] concluded that given the same average geochemical parameters, different mineral spatial patterns resulted in different pore-scale flow patterns and concentration gradients that impacted bulk dissolution rates. Heterogeneities in both reactive mineral distributions and the locations of advection- and diffusion-controlled zones relative to CO_2 injection sites are expected to be key drivers of permeability and porosity changes governing long-term injectivity.

Reactive transport models have been applied extensively to study CO_2 storage in sedimentary basins in the context of caprock stability, CO_2 plume migration, permeability evolution, and wellbore integrity, for example, refs 15−22. Such models are critical to advancing experimental findings given the time and spatial constraints of lab-scale studies.[21] Because CO_2 storage in basalt is a relatively new pursuit compared with storage in deep saline aquifers, most research efforts have yet to substantially integrate numerical modeling. Several studies have included reaction path models, which capture a sequence of chemical or mineralogical states and may incorporate kinetics but do not explicitly consider transport processes.[23] For instance, Marini et al.[24] carried out reaction path modeling of CO_2 injection in continental flood basalt aquifers, predicting dramatic porosity reductions due to sequential precipitation of chalcedony, kaolinite, minor amounts of goethite, and carbonates dominated by dolomite. In reaction path models of volcanic flood basalts, Schaef et al.[25] found that precipitation of clays and chalcedony preceded carbonate formation, which was delayed by reductions in available reactive surface area led by basaltic glass and clinopyroxene dissolution. The authors further noted that carbonate accumulation may affect in situ mineralization efficiency by limiting mass transport across mineral interfaces.[25] More recently, Paukert et al.[26] developed reaction path models for peridotites and demonstrated that anthropogenic CO_2 injection significantly enhanced both the amount of CO_2 mineralized in situ and carbonation efficiency relative to natural systems.

Batch experiments on olivines and basalts have also been supplemented with reaction path models to predict geochemical alterations and reaction product formation,[27−29] but few experimental or modeling efforts have incorporated transport components. Giammar et al.[11] created a reactive transport code to simulate chemical gradients resulting from dissolved inorganic carbon diffusion into packed beds of forsterite. At field scale, Aradottir et al.[30] built 2D and 3D reservoir models for the CarbFix pilot project in Iceland, where CO_2 from the Hellisheidi power plant has been coinjected with formation waters in a nearby basalt flow since 2012.[30] The results indicate mineral carbonation in basalts represents a viable CO_2 sequestration option and provide valuable feedback to optimize injection site management.[30] However, simplifications necessary to run efficient field-scale models, such as the use of volume-averaged subsurface properties, preclude the isolation of parameters governing carbonation reactions at local scales.

The specific objective of this work was to develop a predictive framework for evaluating the roles of transport limitations and mineral spatial distributions on the location and extent of mineral carbonation reactions under conditions relevant to CO_2 injection in basalts. Advection- and diffusion-controlled systems were modeled using the reactive transport code CrunchTope,[31] which has recently been applied to simulate flow of CO_2-acidified fluids through fractures in carbonates,[32] sedimentary host rocks,[16,33] and wellbore cements.[22,34] Effluent chemistry data from high-temperature, high-pressure flow-through experiments served as a benchmark for model calibration. The fracture surfaces from these reacted cores were segmented into discrete mineral grids aligning with the dimensions of model domains in CrunchTope through a series of imaging techniques. Simulated injection of CO_2-acidified brine was compared between this mineral distribution from an actual basalt sample and random spatial distributions of the same volume-averaged composition to assess whether mineral heterogeneities directly impact carbonation efficiency. We demonstrate the utility of this integrated experimental and modeling approach for identifying key controls on the favorability of secondary mineral precipitation and extending lab-scale results to elucidate implications for long-term CO_2 storage.

2. MATERIALS AND METHODS

2.1. Reactive Transport. All models were developed in CrunchTope, a multicomponent reactive transport code that has been applied to a variety of environmental problems involving flow through porous media.[31] Simulations were conducted using the global implicit approach, where time steps are extended as the system approaches steady state to enhance computational efficiency.[31] Additional details on the code's capabilities, limitations, and governing equations are available in the user's manual (available for download from www.csteefel.com).

Mineral reactions are modeled based on transition state theory assuming continuous reversibility between dissolution and precipitation at equilibrium. Reaction rate constants at 100 °C, the temperature applied in all models considered here, were calculated based on selected literature values for the reaction rate constant at 25 °C and activation energy according to the Arrhenius relationship:

$$k = k_{25}\exp\left[\frac{-E_a}{R}\left(\frac{1}{T} - \frac{1}{298.15}\right)\right] \quad (1)$$

Reaction pH dependence was incorporated by summing adjusted rate constants for acid (H), neutral (neu), and basic (OH) mechanisms, where n and m are the partial orders of reaction with respect to H^+ and OH^-, respectively:

$$k_{rxn} = a_H{}^n k_H + k_{neu} + a_{OH}{}^m k_{OH} \quad (2)$$

DOI: 10.1021/acs.est.7b00326
Environ. Sci. Technol. 2017, 51, 9352−9362

Table 1. Summary of Primary and Secondary Mineral Kinetic Data and Reactive Surface Areas

		acid mechanism		neutral	basic mechanism		SSA (m^2/g)	
mineral	initial volume fraction (%)	log k, 100 °C (mol/m^2/s)	n^{H+}	log k, 100 °C (mol/m^2/s)	log k, 100 °C (mol/m^2/s)	n^{OH-}	calculated (geometric)[a]	selected[b]
Primary Minerals								
diopside	22	−2.97[44]	0.71[44]	−9.68[44]			0.0148	0.0034[c]
albite	12	−6.47[45]	0.50[45]	−9.66[45]			0.0225	0.0225
anorthite	18	−6.47[45]	0.50[45]	−9.66[45]			0.0225	0.0225
antigorite	11	−7.54[46]	0.45[46]	−10.1[47]			0.0165	0.18
forsterite	1	−4.48[44]	0.47[44]	−7.85[44]			0.0148	0.018
fayalite	3	−3.53[d]	0.47[44]	−9.48[44]			0.0148	0.0018
K-feldspar	33	−7.63[44,45]	0.50[44]	−11.29[44]	−17.9[44]	−0.823[44]	0.019	0.019
Secondary Minerals								
calcite	0	0.21[44]	1.0[44]	−4.98[44]				0.037[48]
magnesite	0	−5.87[44]	1.0[44]	−8.51[44]				0.0662[48]
siderite	0	−1.76[49]	0.90[49]	−6.69[45]				0.105[50]
SiO_2(am)	0			−6.92[51]				0.0225[52]
kaolinite	0	−8.99[44]	0.777[44]	−12.4[44]	−16.4[44]	−0.472[44]		8.16[53]

[a]Geometric surface areas calculated as smooth spheres based on average phenocryst grain sizes (see SI). [b]Some SSA values were tuned from the calculated geometric values to optimize fit to experimental effluent data. [c]In the initial calibration, 18% of the diopside was added with a higher SSA of 0.11 m^2/g to match rapid initial dissolution from finer surface particles (see SI). [d]Reaction rate adjusted to fit Fe data by setting k_{2S} to that of forsterite (see SI).

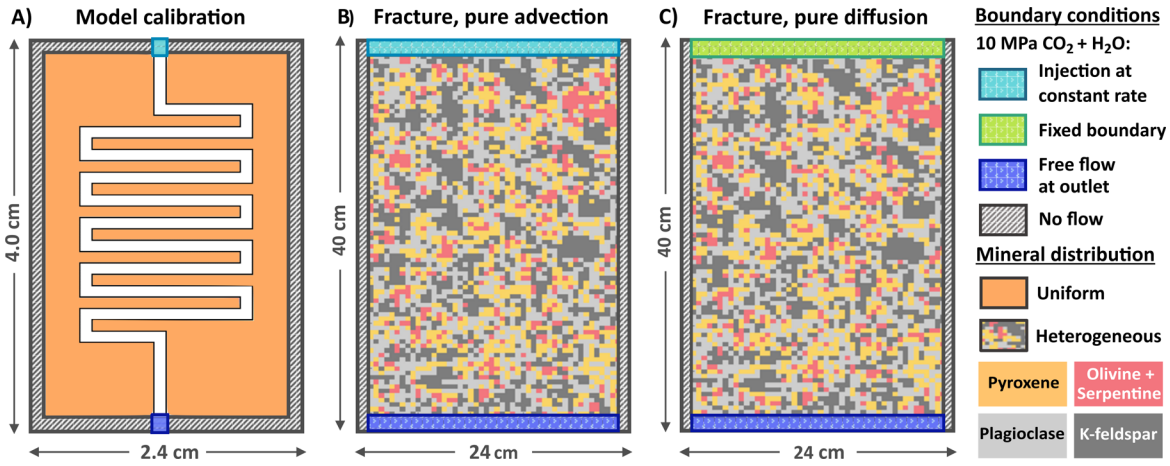

Figure 1. Conceptual model domains for (A) initial calibration simulating flow-through experiments with uniform mineralogy; (B) pure advection in a heterogeneous open fracture; and (C) pure diffusion in a heterogeneous open fracture.

For each mineral, the reaction rate constant, total surface area (A), and saturation index are then used to calculate the overall reaction rate at each time step:

$$r = -Ak_{rxn}\left[1 - \frac{Q}{K}\right] \quad (3)$$

While extrapolating to high temperatures may introduce errors in mineral reactivities, specific surface areas are likely the main source of uncertainty in this formulation. Calculated reaction rate constants and literature-reported pH and pOH dependence for all primary and secondary minerals are summarized in Table 1. Note that dolomite was intentionally excluded as a secondary mineral due to its well-established disinclination to precipitate under modern natural conditions despite thermodynamic favorability.[35,36] Quartz was also suppressed due to its slow precipitation kinetics. Under the conditions in this study, solutions supersaturated with respect to SiO_2 would predominantly precipitate amorphous silica, which has a lower interfacial energy and faster nucleation rate than crystalline forms.[37]

2.2. Model Benchmarking. An initial model was developed to simulate the core-flooding experiment presented by Adeoye et al.[38] involving flow of CO_2-acidified brine through a serpentinized basalt core under high temperature (100 °C) and pressure (10 MPa P_{CO2}). The core was divided into two halves with one containing a 100 μm-deep etched fracture pathway designed to extend fluid residence time (Figure 1). The surface of this fractured half was discretized into a grid of 48 × 80 cells, each 0.5 × 0.5 mm. The height of each cell (0.011 mm) was calculated to match the residence time of the flow-through experiments (0.0046 h). Although the actual physical domain consists of an open fracture between two basalt surfaces, 2D models consider each cell as a porous media with bulk volumes of mineral and void space. To simulate the fracture walls and provide sufficient mineral for reaction, the fracture porosity was set to 90% in the code.[33] Some previous studies have assigned fracture porosities of 100% to examine fracture cross sections,[16,22] but the incorporation of minerals in the fracture here was necessary to simulate a 2D plane of fluid surrounded by reactive surface area. While the actual porosity

DOI: 10.1021/acs.est.7b00326
Environ. Sci. Technol. 2017, 51, 9352−9362

of the basalt samples is low (~1%),[39] the modeled matrix porosity was set to 5% to prevent rapid pore clogging. Porosity is allowed to evolve during simulations in accordance with changes in mineral volume fractions. To match experimental conditions, water equilibrated with 10 MPa CO_2 was injected into the fracture pathway at a rate of 5 mL/h. CO_2 fugacity was computed directly in the code using the empirical formulation provided by Duan and Sun.[40] Longitudinal and transverse dispersivities were set to 10% of the flow path length (0.023 m). The diffusion coefficient was fixed at 7.5×10^{-9} m^2/s, corresponding to the mean value for CO_2 in water at 100 °C reported by Cadogan et al.[41]

Experimental effluent chemistry data served as a benchmark for adjusting uncertain model input parameters. Because reactive transport models are highly sensitive to mineral reactive surface areas, which are also generally the source of greatest uncertainty,[42] values are typically adjusted from calculated geometric or measured BET surface areas to fit experimental data.[16,30] Here, specific surface area (SSA) was first calculated assuming spherical geometry, using average diameters corresponding to phenocryst grain size distributions from preliminary characterization of the reacted cores.[38,39] These geometric SSA values were then fine-tuned where necessary to match effluent chemistry for divalent cations (Ca^{2+}, Mg^{2+}, Fe^{2+}) at the outlet of the model domain. Aligning model outputs with experimental silica and minor cation (Na^+, K^+) concentrations required altering mineral stoichiometry and reaction rates and was ultimately neglected to avoid over-constraining the model. Initial primary mineral volume fractions were adjusted to within 2% of values derived from previously reported wavelength dispersive spectroscopy analyses[39] to optimize the fit.

While Steefel and Van Cappellen[37] developed a reactive flow model incorporating expressions for heterogeneous nucleation, growth, and Ostwald ripening, nucleation has not been fully coupled with reactive transport codes. Fritz et al.[43] modeled clay nucleation and growth but acknowledged that significant uncertainties in input parameters such as interfacial free energies and pre-exponential constants in the nucleation rate equation limit the application of quantitative results. In the absence of sufficient nucleation kinetic data for the secondary mineral phases in our system, precipitation is initiated through a threshold volume fraction. All secondary minerals are assigned initial volume fractions of 0 and volume fraction thresholds of 10^{-5} to calculate bulk surface area until the volume fraction threshold is exceeded; thereafter, the precipitate's surface area is updated according to its calculated volume fraction and reported BET surface areas (Table 1). SSA values for all minerals used in the models are included in Table 1, while additional details regarding the calculation and selection of input parameters are provided in the Supporting Information (SI).

After achieving calibration using data from a high-temperature, high-pressure flow-through experiment with a serpentinized basalt sample, the model was validated using data from a flow-through experiment conducted under the same conditions (100 °C, 10 MPa CO_2, 5 mL/h) but with an unserpentinized basalt core. Mineral volume fractions of pyroxene and olivine were altered to account for slight differences in bulk mineralogy, and the reactive surface areas of diopside and forsterite were reduced by half to match lower effluent Ca and Mg concentrations. A full accounting of the inputs and results is included in the SI. Because both samples produced similar experimental effluent data and the effect of bulk composition was not the focus of this work, the mineralogy of the serpentinized basalt used in the initial calibration is applied for all models.

2.3. Mapping Mineral Spatial Distributions. Discretized mineral grids were developed for heterogeneous models using an approach similar to that demonstrated by Ellis and Peters,[54] which is detailed in the SI (section S4) and summarized here. Energy-dispersive spectroscopy (EDS) was coupled with backscattered electron (BSE) images to identify specific minerals in a reacted basalt core, which were then mapped to features in X-ray computed tomography (xCT) scans. Mineral spatial distributions along the fracture path were obtained by first coarsening an image of the fracture to align with the model domain by assigning one average pixel intensity to each 0.5 × 0.5 mm block. This image was segmented into four discrete mineral phases (pyroxene; plagioclase; serpentinized; and unserpentinized olivine; and K-feldspar) based on ranges in pixel intensities corresponding to each mineral identified in the xCT/EDS analysis. Conditions for each mineral group were created in CrunchTope to match the specific minerals selected in the uniform models (Table 1), and each cell was assigned one of four mineral conditions based on the processed CT image. Relative fractions of each mineral aligned well with those applied in the uniform model based on WDS analyses. Example BSE/EDS images and a schematic overview of the segmentation process are also provided in the SI.

2.4. Hypothesis-Driven Model Development. Previous flow-through experiments served as an effective benchmark but were not intended to constrain modeling efforts. To this end, an idealized uniform fracture was taken as the domain for subsequent models designed to isolate the roles of transport and mineral heterogeneities in controlling dissolution and precipitation reactions. Because the small volume of the domain used in calibration induced rapid mineral dissolution and exhaustion due to low mineral volumes, all cells were scaled up to 0.5 × 0.5 × 0.5 cm, effectively increasing the domain volume by 3 orders of magnitude, to facilitate comparisons over longer time frames.

Two models were developed to investigate the role of transport limitations: one considering pure advection and one with pure diffusion. The segmented mineral distribution based on an actual core sample was used for these models to explore coupled effects of transport and mineral heterogeneities. The mineralogy, domain setup, and boundary conditions are illustrated in Figure 1. Both conditions allowed free flow at the lower boundary, whereas the upper boundary supplied CO_2-saturated water (equilibrated at 10 MPa P_{CO2}) through constant injection for the advection model and a Dirichlet (fixed concentration) boundary for diffusion. Pure advection models were developed by setting the injection rate to achieve each of 8 selected residence times (6, 12, 24, 48, 96, 144, 192, and 288 h) in the fixed domain volume. The fixed diffusion coefficient used in calibration (7.5×10^{-9} m^2/s) was applied for pure diffusion. Each grid cell was assigned a porosity of 60% to provide sufficient mineral volumes in the domain for continued reaction over longer time frames. The remaining mineral fraction (40%) essentially consisted of two "layers": 70% contains only the mineral allocated to that cell in the segmentation, and 30% is comprised of an underlying uniform mineral distribution corresponding to the bulk mineralogy. This approach reasonably captures mineral heterogeneities while allowing for continued dissolution of the underlying rock

DOI: 10.1021/acs.est.7b00326
Environ. Sci. Technol. 2017, 51, 9352−9362

matrix if reactive mineral cells are depleted during simulations. As previously noted, a cell containing both mineral and fracture is viewed as a porous medium in 2D modeling; thus, applying a lower porosity to the fracture than that used in model calibration essentially increases the amount of surrounding rock captured by the domain. Note that in contrast to the dual porosity models developed for calibration with zones of fracture and matrix, the models developed here to investigate the roles of transport limitations and heterogeneities have a single uniform porosity of 60% to simulate a fracture surrounded by reactive surface area.

To isolate the effects of mineral heterogeneity on the extent and location of carbonation, transport conditions were held constant while additional simulations were run using random mineral grids with comparable domain-averaged compositions. These models were set up identically to those in Figure 1b and c with varying realizations of mineral spatial distributions, including models with larger clusters of reactive minerals to evaluate whether highly localized concentrations of certain minerals affect the extent of carbonation compared with more even allocation across the domain. A summary of transport conditions and mineral distributions applied to each model included in this study is provided in Table 2. Segmented mineral distributions refer to those obtained by segmenting the fracture surface of a serpentinized basalt core used by Adeoye et al.,[38] while random distributions were generated in MATLAB using the same volume-averaged fractions of primary minerals. Two types of "random" grids were tested: grids where the mineral assigned to every cell was truly random and grids where larger mineral clusters were randomly generated within the domain to emphasize preferential precipitation of certain secondary minerals on specific primary sites. Because simulations with these random distributions resulted in negligible differences in the total volume of carbonates formed at a given time step, only one of these grids is presented in the results for comparison with the segmented grid from the actual serpentinized basalt sample. Results for other selected random grids are included in the SI.

Table 2. Summary of Key Conditions for Models Discussed in This Study

model[a]	transport conditions	mineral distribution
TA1	pure advection with τ = 6, 12, 24, 48, 96, 144, 192, and 288h	segmented (1)
TD1	pure diffusion	segmented (1)
SA1	pure advection with τ = 288h	segmented (1)
SA2	pure advection with τ = 288h	random (2)
SD2	pure diffusion	random (2)

[a]First letter corresponds to the model purpose: investigating transport conditions (T) or mineral spatial distributions (S); second reflects transport conditions (advection or diffusion); and third indicates the spatial distribution used (1 for the segmented grid from an actual core and 2 for a random distribution with the same volume-averaged mineralogy).

2.5. Simulations with Additional Secondary Silicates. Previous work has suggested secondary silicate precipitation may limit carbonation efficiency. Experimental and modeling studies have demonstrated precipitation of clays and zeolites over a range of conditions relevant to CO_2 storage that could compete with carbonates for divalent cations.[e.g.30,55−58] In packed bed experiments with the same basalts and similar conditions as this study, siderite, zeolite, lizardite, and trace amounts of amorphous silica were observed.[59] To evaluate the influence of Ca-, Mg-, and Fe-bearing secondary silicates, the advection and diffusion models developed to investigate transport limitations were run with additional secondary minerals: smectite (modeled as 4 montmorillonite end-members), biotite (annite and phlogopite), and zeolite (laumontite). Further details on inputs and results from these simulations are provided in the SI, while the implications are presented in Section 3.4.

3. RESULTS AND DISCUSSION

3.1. Model-Experiment Correlation. As described in Section 2.4, the initial model domain and conditions were aligned with a series of flow-through experiments presented by Adeoye et al.[38] Model trends in major dissolved cations were benchmarked to measured effluent concentrations over the experimental time frame. Figure 2 demonstrates that the model reasonably captures the dissolution of the key divalent cations; additional cation comparisons are included in the SI. Note that a fraction of the diopside in the calibrated model is assigned a higher specific surface area to capture initial Ca and Mg concentration spikes, presumably resulting from rapid initial dissolution of fine-grained surface particles in the flow-through experiment. As noted in the SI, only one SSA for diopside is used in subsequent models. Simulations overestimate initial silica concentrations because cations were preferentially released from the bulk silica matrix during the experiment. The model also underestimates concentrations of monovalent cations, possibly due to incongruent dissolution of feldspars. Despite these limitations, explicit calibration to experimental

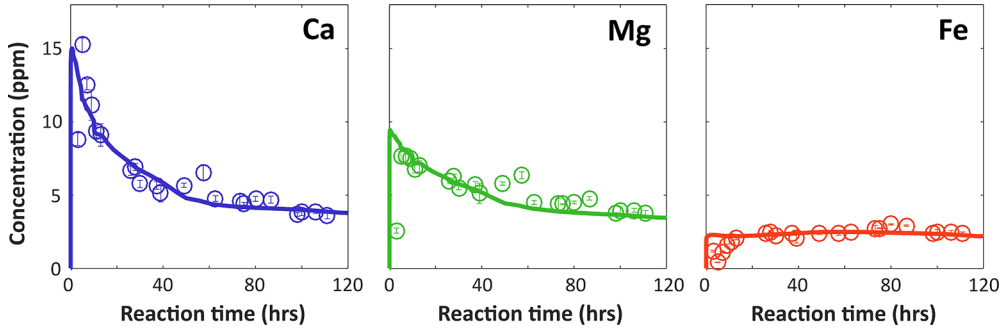

Figure 2. Comparison of calibrated model results with experimental effluent chemistry data from a core-flooding experiment conducted at 100 °C under constant flow (5 mL/h) of CO_2-acidified brine (10 MPa P_{CO2}) through a serpentinized basalt sample.

DOI: 10.1021/acs.est.7b00326
Environ. Sci. Technol. 2017, 51, 9352−9362

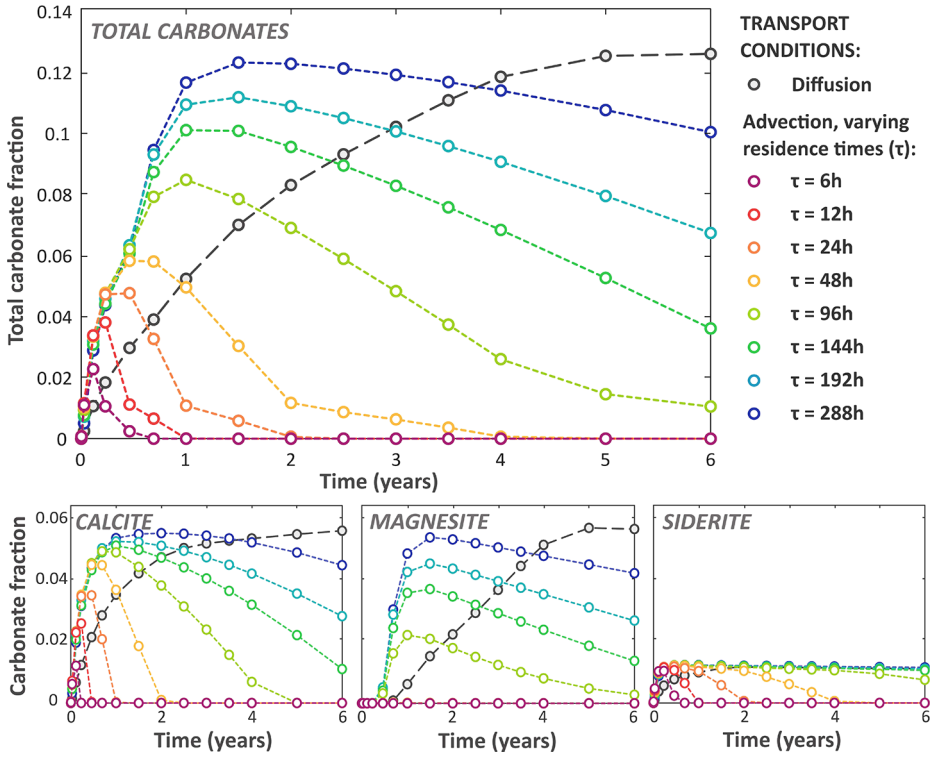

Figure 3. Total fraction of carbonates formed (presented as cm^3 of carbonate minerals per cm^3 of the modeled fracture domain) as a function of time for nine selected transport conditions: pure diffusion and pure advection under 8 different hydraulic retention times. Subfigures indicate individual contributions from calcite, magnesite, and siderite to total carbonation.

results was intentionally avoided to provide a representative but not overly constrained basis for model development.

3.2. Role of Transport Limitations. To evaluate the effects of transport conditions on carbonation efficiency, simulations were conducted for pure diffusion and pure advection under eight different hydraulic retention times using the domains illustrated in Figure 1b and c. Discrete outputs of carbonate volume fractions, defined as the volume of carbonates formed per unit volume of porous media in the domain, are plotted as a function of simulation time in Figure 3. Carbonation in the pure advection systems is controlled by residence time, and the "optimal" residence time for maximum carbonate precipitation depends on the time frame of interest. For instance, advection promotes more carbonate precipitation than diffusion in the first 1−2 years after commencing CO_2 injection, with lower flow rates becoming more favorable over longer times as carbonates are able to accumulate. Shorter retention times (corresponding to faster flow) lead to greater initial carbonation driven by rapid dissolution, but these carbonates quickly redissolve as continued CO_2 injection increases the acidity of surrounding fluids and reactive primary mineral phases are depleted. Calcite dissolution tracked with diopside depletion at the inlet, leaving behind feldspars that react too slowly to provide sufficient buffering to offset the drop in pH and sustain carbonate precipitates. Qiao et al.[60] observed similar behavior in numerical modeling of CO_2 flooding in carbonate reservoirs, whereby instantaneous drops in pH due to CO_2 injection outpaced the rise in pH from mineral dissolution that occurred over longer time frames. Although the models do not predict reprecipitation in the absence of more rapid pH buffering, these redissolved cations would likely reprecipitate further downstream where the CO_2 front has not advanced far enough to reduce the pH below carbonate saturation. These results are partially driven by the size of the model domain but indicate that rapid and continuous CO_2 injection at field scale could erode carbonates formed along main flow paths, particularly if precipitation is highly localized in small clusters. If reactive minerals are abundant near wellbores, high flow rates and high CO_2 partial pressures may favor continued dissolution and inhibit precipitation.

While carbonation efficiency (i.e., the amount of carbonates formed with respect to the amount of divalent cation-bearing minerals dissolved) is highest under diffusive mass transport conditions, greater total volumes of carbonates are formed under advective flow for early time frames (1−2 years) because more divalent cations are available. Carbonates form more slowly in the diffusion model but are more stable, reaching quasi steady-state volume fractions over longer time frames and redissolving minimally with continued CO_2 penetration. Diffusion also lengthens surface reaction times, maintaining favorable pH levels for carbonate saturation and allowing for greater precipitation over time scales on the order of years. Unless CO_2 injection occurs in areas with high abundances of pre-existing reactive minerals (e.g., calcite), it will likely generate strong advective conditions near the wellbore that result in net dissolution, while most carbonation will occur in low-porosity zones surrounding main flow channels or dead-end fractures further from the wellbore where transport is limited by diffusion.

After two years, most of the dissolved calcium is contained in calcite (87%) under diffusive conditions, while the fraction of carbonated Ca decreases with decreasing residence time for the advection cases. All of the dissolved Ca is released from the domain (i.e., none remains trapped in carbonates) for residence times less than or equal to 24 h. Additionally, all diopside in the model domain dissolves after one year, but smaller amounts of

DOI: 10.1021/acs.est.7b00326
Environ. Sci. Technol. 2017, 51, 9352−9362

Ca are still released from anorthite at slower rates. Extended retention times prolong diopside depletion and allow for greater carbonate accumulation, as continued dissolution of reactive minerals releases silicates rapidly enough to provide pH buffering. Although all tested conditions initially yielded net dissolution, the diffusion model achieved net precipitation within 6 weeks. In this case, the contribution of carbonates to the total volume of secondary precipitates declined from 92% at 10 days to 42% after 6 years as amorphous silica and kaolinite accumulated. Similar trends were observed under slow-flow advection, but residence times of 48h or less resulted in net dissolution after 6 years. Note that while the model does not account for effects of passivating layers, secondary precipitation of amorphous silica predicted in all models could reduce carbonation efficiency in actual reservoirs by obstructing CO_2 transport to mineral surfaces and reducing permeability along flow paths.[29] Amorphous silica layers have also been shown to kinetically control olivine dissolution and significantly inhibit carbonation rates at 90 °C.[61]

The subfigures in Figure 3 track the contributions of calcite, magnesite, and siderite to the total carbonate fractions at each time step, illustrating how calcite controls carbonation at early time frames while contributions from magnesite and siderite become more significant with continued CO_2 injection. Note that due to uncertainties in actual carbonate precipitation rates, these results are limited by the assumption that carbonate formation is kinetically controlled, i.e. dissolution and precipitation reactions proceed reversibly according to the same reaction rates. Nucleation kinetics and crystal growth mechanisms (e.g., Ostwald ripening) will also be key considerations in actual systems where critical degrees of supersaturation are required to initiate precipitation.

Because calcite has the fastest kinetic parameters in the model, it forms most rapidly under pure advection with short retention times but also redissolves quickly because reactive minerals are depleted and reaction products are transported out of the domain before significant pH buffering can occur. Magnesite consistently had the highest saturation index across the domain (see SI) but only formed at retention times greater than or equal to 96 h due to kinetic limitations. Diopside contributed the most to mineral dissolution, providing both Ca and Mg for carbonation, but the fast reaction rate of calcite relative to magnesite leads to preferential calcite precipitation given sufficient Ca availability. The advective models predict magnesite will redissolve around the same time as calcite but at a slower rate. Siderite formed to a lesser extent due to kinetic limitations but was more resistant to redissolution over longer time frames. The preferential formation of calcite over other carbonates is consistent with prior work that found calcite growth rates exceeded those of magnesite by 6 orders of magnitude[62] and siderite by 8 orders[63] under equivalent conditions and saturation indices. Such studies have attributed the differences in carbonate precipitation kinetics to higher surface charge densities for siderite and magnesite, as the smaller ionic radii of Fe^{2+} and Mg^{2+} relative to Ca^{2+} require higher activation energies to initiate dehydration and subsequent precipitation.[63]

3.3. Role of Mineral Spatial Distribution. Modeling results for various spatial realizations of the same bulk mineralogy indicate that mineral heterogeneities may control the location of secondary precipitation but negligibly impact the extent. Figure 4 compares the volume fractions of carbonates formed after 2 years for the segmented mineralogy from an actual core sample with a random distribution of comparable bulk composition. While the figures elucidate the effects of heterogeneity on carbonate locations, the variation in total volumes of carbonates formed in the fracture domain over two years attributable to slight differences in primary mineralogy was only 4%. Additional simulations (see SI) using random distributions with the same mineral fractions as the random grids in Figure 4 produced carbonate volumes within 2−3% of each other at each time step over 10 years, even when reactive minerals were concentrated in large clusters. Despite negligible influence on precipated carbonate volumes, the locations of primary minerals govern the location of carbonate precipitation, which occurs on reactive mineral phases containing the requisite divalent cations. Calcite forms preferentially on pyroxene and to a lesser extent on plagioclase; magnesite is more uniformly distributed but forms in greater volumes on pyroxene and olivine grains; and siderite is localized on olivine, the only Fe-bearing mineral included (Figure 4). These observations indicate that for given flow conditions and volume-averaged primary mineral abundances, mineral heterogeneities will not impact the amount of carbonates formed but will control local solution concentration, which will influence the location of secondary precipitates. In actual systems, heterogeneous nucleation may also contribute to preferential precipitate formation on specific primary minerals.

As expected, pH also governs which carbonates precipitate through its effect on saturation indices. In the simulations, calcite redissolved when reactive minerals were depleted and the pH dropped below 4.5, while siderite was still able to form where pH was above 4. This reflects observations in previous experiments with the basalt samples used to calibrate the model, where siderite was the most favorable carbonate precipitate under low pH conditions given comparable amounts of available Ca^{2+}, Mg^{2+}, and Fe^{2+}.[38] Here, the preferential formation of siderite bands behind the dissolving calcite and magnesite fronts likely occurs because sufficient CO_2 and divalent cations are available for precipitation, but the pH has fallen to a point where only siderite reaches saturation. While magnesite generally had the highest saturation index of the three carbonates (see section S5 of SI), calcite formed more readily due to the kinetic limitations discussed in Section 3.2 and was strongly localized on pyroxene grains that rapidly released Ca^{2+}. Because the difference in reaction rates between the two minerals serving as Ca sources (pyroxene and plagioclase) was far greater than for the minerals contributing Mg (pyroxene and olivine), Mg dissolution and subsequent magnesite precipitation was more uniformly distributed while calcite precipitation was highly localized and coincident with rapid Ca^{2+} release from pyroxene grains.

Models SA1 and SA2 in Figure 4 highlight the influence of transport conditions on the role of heterogeneity. Under advective flow, large calcite precipitates that formed on large contiguous pyroxene clusters dissolved slower than the more uniformly distributed surrounding calcite grains. These larger grains also served as pH buffers to delay model-predicted redissolution. This “armoring” effect was less pronounced for pure diffusion because more dissolved silicates were retained with longer reaction times, providing pH buffering for carbonate accumulation and preventing redissolution. The segmented mineral grid, which contained few large mineral clusters, also dissolved more uniformly. Thus, mineral spatial distributions impact where minerals dissolve and carbonates

DOI: 10.1021/acs.est.7b00326
Environ. Sci. Technol. 2017, 51, 9352−9362

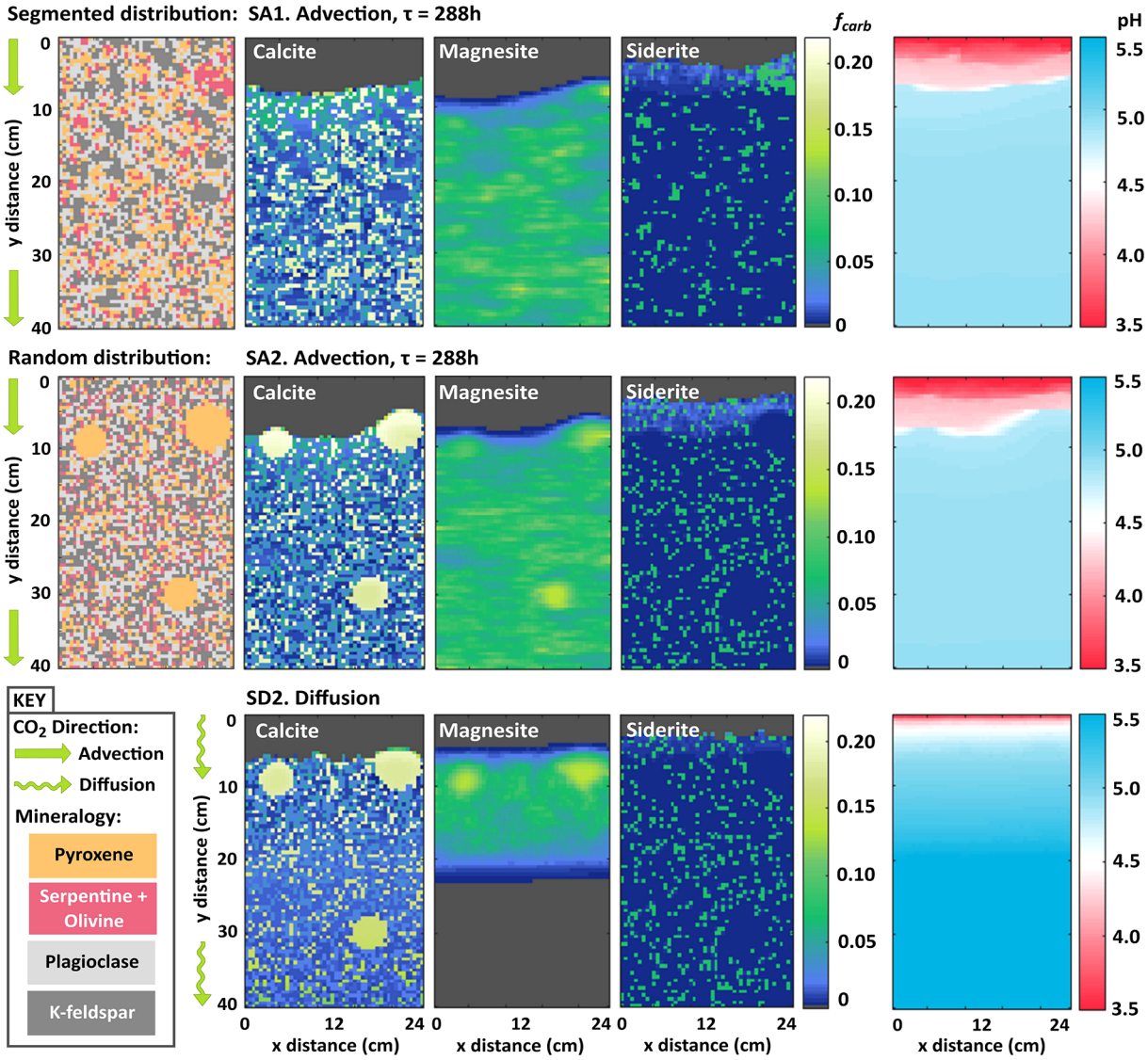

Figure 4. Spatial distributions of carbonation (expressed as carbonate fractions, f_{carb}, which represent cm^3 of carbonate per cm^3 of domain volume) across the model domain after 2 years of injection of CO_2-acidified brine for two selected heterogeneous distributions with comparable bulk mineral compositions: (1) segmented core sample from flow-through experiments and (2) random distribution with larger pyroxene clusters. Results for two flow conditions, low-flow advection and diffusion, are also compared for grid 2.

precipitate, but the evolution of these reactions will also be influenced by transport regimes. In combination, the results indicate that small-scale heterogeneities may be insignificant, while the combined interactions of transport limitations, geochemical gradients (e.g., in pH), and bulk mineralogy will likely control the extent of mineral carbonation induced by CO_2 injection in basalt reservoirs.

3.4. Role of Competition with Secondary Silicates. In models run with additional secondary silicates, the uptake of dissolved cations that had previously diffused out of the domain in clay minerals led to more rapid pore clogging (within 8 years for pure diffusion and 3.5−8 years for slower advection). For faster advection (τ of 24 h or less), dissolution predominated over precipitation and pores remained open after 10 years. While smectite formed quickly and was less localized than carbonates with respect to primary minerals, 87% of Mg was contained in magnesite after 2 years. Essentially no zeolite or biotite precipitated for any transport condition. Further details and results are provided in Section S5 of the SI.

The models indicate competition with clays for divalent cations will not pose a significant direct threat to carbonation under these conditions, as smectite precipitation reduced total predicted carbonate volumes across the model domain by 3−6% after 2 years due primarily to Mg uptake into montmorillonite. In batch experiments on basaltic glass, Hellevang et al.[58] observed smectite growth from 80 to 150 °C and attributed a lack of Mg- and Fe-carbonates not to competition with clays for divalent cations, but to the potential for smectite coatings to create an energy barrier to nucleation combined with slow carbonate growth kinetics. Even if smectite does not directly impact carbonation by depleting divalent cations or impeding nucleation, our models indicate early clay precipitation could still clog narrow fractures and pore throats, potentially reducing permeability and CO_2 injectivity.[58] Such physical alterations were not considered in this study but will be critical in predicting ultimate CO_2 trapping potentials of basalt reservoirs.

DOI: 10.1021/acs.est.7b00326
Environ. Sci. Technol. 2017, 51, 9352−9362

Environmental Implications. Reactive transport models developed based on bench-scale experiments were extended to isolate the roles of transport limitations and mineral spatial distributions in controlling mineral carbonation reactions in fractured basalts. Under pure advective flow, carbonates eventually redissolved with continued injection as the pH dropped below saturation thresholds and primary reactive silicates needed to buffer injected fluids were depleted. While mineral exhaustion will not be an issue at field scale, depletion of reactive mineral zones along fracture surfaces could leave less reactive altered layers that limit mineral dissolution, allowing the pH to drop low enough that carbonate precipitation is no longer favorable and precipitates are susceptible to redissolution. These results indicate that injectivities should be carefully assessed at sites with low abundances of reactive minerals to ensure stable trapping is achieved. Strong advective conditions may prevent carbonation near wellbores and drive a domino effect of carbonate dissolution and reprecipitation along CO_2 flow paths. This chain could promote appreciable carbonation along main conduits in the absence of flow blockage, but in terms of storage security, long-term carbonation will likely occur in diffusive regions within the bulk matrix and in dead-end fractures.

In the models presented here, reactive surface area is assumed to be proportional to the bulk surface area and is updated according to changes in mineral volume fractions. In reality, this may be an oversimplification due to changes in growth site densities at mineral surfaces over time.[37] The SSAs used to compute mineral reactive surface areas are also a source of both uncertainty and model sensitivity. Furthermore, heterogeneous nucleation may accelerate carbonate formation on certain substrate minerals. Incorporating a more robust means of capturing nucleation events and subsequent crystal growth in future modeling efforts will be critical to predicting field-scale rates and extents of mineral carbonation in basalts. Bulk reservoir mineralogy and the chemical composition of resident fluids will also govern the extent of carbonation. For instance, the fact that formation waters surrounding the CarbFix site were near equilibrium with respect to calcite limited redissolution of calcite precipitates with continued CO_2 injection.[7] Matter et al.[7] also noted that most carbonates likely precipitated in the porous matrix outside advective flow paths, consistent with model predictions of precipitation in lower porosity zones provide greater rock:water ratios and longer reaction times. Coupling field-scale efforts with efficient reactive transport models can elucidate how subsurface CO_2-water-rock reactions enhance or inhibit carbonation efficiency. Such insight will be crucial in predicting long-term mineral carbonation rates to optimize injection site selection.

■ ASSOCIATED CONTENT

Supporting Information

The Supporting Information is available free of charge on the ACS Publications website at DOI: 10.1021/acs.est.7b00326.

Additional details on calculating specific surface area (S1), model calibration (S2) and validation (S3), mapping mineral spatial distributions (S4), and supplemental modeling results (S5) (PDF)

■ AUTHOR INFORMATION

Corresponding Author

*Phone: 734-763-5470; fax: 734-764-4292; e-mail: brellis@umich.edu.

ORCID

Anne H. Menefee: 0000-0003-2740-3208
Daniel E. Giammar: 0000-0002-4634-5640
Brian R. Ellis: 0000-0002-7253-4285

Notes

The authors declare no competing financial interest.

■ ACKNOWLEDGMENTS

This work is supported by the U.S. Department of Energy via Award DE-FE0023382.

■ REFERENCES

(1) Harvey, O. R.; Qafoku, N. P.; Cantrell, K. J.; Lee, G.; Amonette, J. E.; Brown, C. F. Geochemical implications of gas leakage associated with geologic CO_2 storage— A qualitative review. *Environ. Sci. Technol.* **2013**, *47* (1), 23−36.

(2) Matter, J. M.; Kelemen, P. B. Permanent storage of carbon dioxide in geological reservoirs by mineral carbonation. *Nat. Geosci.* **2009**, *2* (12), 837−841.

(3) Gislason, S. R.; Wolff-Boenisch, D.; Stefansson, A.; Oelkers, E. H.; Gunnlaugsson, E.; Sigurdardottir, H.; Sigfusson, B.; Broecker, W. S.; Matter, J. M.; Stute, M. Mineral sequestration of carbon dioxide in basalt: A pre-injection overview of the CarbFix project. *Int. J. Greenhouse Gas Control* **2010**, *4* (3), 537−545.

(4) Schaef, H. T.; McGrail, B. P. Dissolution of Columbia River Basalt under mildly acidic conditions as a function of temperature: Experimental results relevant to the geological sequestration of carbon dioxide. *Appl. Geochem.* **2009**, *24* (5), 980−987.

(5) Sissmann, O.; Brunet, F.; Martinez, I.; Guyot, F.; Verlaguet, A.; Pinquier, Y.; Daval, D. Enhanced olivine carbonation within a basalt as compared to single-phase experiments: Reevaluating the potential of CO_2 mineral sequestration. *Environ. Sci. Technol.* **2014**, *48* (10), 5512−5519.

(6) McGrail, B. P.; Schaef, H. T.; Spane, F. A.; Cliff, J. B.; Qafoku, O.; Horner, J. A.; Thompson, C. J.; Owen, A. T.; Sullivan, C. E. Field validation of supercritical CO_2 reactivity with basalts. *Environ. Sci. Technol. Lett.* **2017**, *4* (1), 6−10.

(7) Matter, J. M.; Stute, M.; Snaebjornsdottir, S. O.; Oelkers, E. H.; Gislason, S. R.; Aradottir, E. S.; Sigfusson, B.; Gunnarsson, I.; Sigurdardottir, H.; Gunnlaugsson, E.; et al. Rapid carbon mineralization for permanent disposal of anthropogenic carbon dioxide emissions. *Science* **2016**, *352* (6291), 1312−1314.

(8) Peuble, S.; Godard, M.; Luquot, L.; Andreani, M.; Martinez, I.; Gouze, P. CO_2 geological storage in olivine rich basaltic aquifers: New insights from reactive-percolation experiments. *Appl. Geochem.* **2015**, *52*, 174−190.

(9) Andreani, M.; Luquot, L.; Gouze, P.; Godard, M.; Hoisé, E.; Gibert, B. Experimental study of carbon sequestration reactions controlled by the percolation of CO_2-rich brine through peridotites. *Environ. Sci. Technol.* **2009**, *43* (4), 1226−1231.

(10) Xiong, W.; Giammar, D. Forsterite carbonation in zones with transport limited by diffusion. *Environ. Sci. Technol. Lett.* **2014**, *1* (8), 333−338.

(11) Giammar, D. E.; Wang, F.; Guo, B.; Surface, J. A.; Peters, C. A.; Conradi, M. S.; Hayes, S. E. Impacts of diffusive transport on carbonate mineral formation from magnesium silicate-CO_2-water reactions. *Environ. Sci. Technol.* **2014**, *48* (24), 14344−14351.

(12) Salehikhoo, F.; Li, L.; Brantley, S. L. Magnesite dissolution rates at different spatial scales: The role of mineral spatial distribution and flow velocity. *Geochim. Cosmochim. Acta* **2013**, *108*, 91−106.

DOI: 10.1021/acs.est.7b00326
Environ. Sci. Technol. 2017, 51, 9352−9362

(13) Li, L.; Salehikhoo, F.; Brantley, S. L.; Heidari, P. Spatial zonation limits magnesite dissolution in porous media. *Geochim. Cosmochim. Acta* **2014**, *126*, 555−573.
(14) Molins, S.; Trebotich, D.; Steefel, C. I.; Shen, C. An investigation of the effect of pore scale flow on average geochemical reaction rates using direct numerical simulation: Effect of pore scale flow on geochemical reaction rates. *Water Resour. Res.* **2012**, *48* (3), W03527.
(15) Deng, H.; Ellis, B. R.; Peters, C. A.; Fitts, J. P.; Crandall, D.; Bromhal, G. S. Modifications of carbonate fracture hydrodynamic properties by CO_2-acidified brine flow. *Energy Fuels* **2013**, *27* (8), 4221−4231.
(16) Wen, H.; Li, L.; Crandall, D.; Hakala, A. Where lower calcite abundance creates more alteration: Enhanced rock matrix diffusivity induced by preferential dissolution. *Energy Fuels* **2016**, *30* (5), 4197−4208.
(17) Nogues, J. P.; Fitts, J. P.; Celia, M. A.; Peters, C. A. Permeability evolution due to dissolution and precipitation of carbonates using reactive transport modeling in pore networks. *Water Resour. Res.* **2013**, *49* (9), 6006−6021.
(18) Xu, T.; Kharaka, Y. K.; Doughty, C.; Freifeld, B. M.; Daley, T. M. Reactive transport modeling to study changes in water chemistry induced by CO_2 injection at the Frio-I Brine Pilot. *Chem. Geol.* **2010**, *271* (3−4), 153−164.
(19) Ilgen, A. G.; Cygan, R. T. Mineral dissolution and precipitation during CO2 injection at the Frio-I Brine Pilot: Geochemical modeling and uncertainty analysis. *Int. J. Greenhouse Gas Control* **2016**, *44*, 166−174.
(20) Bacci, G.; Korre, A.; Durucan, S. An experimental and numerical investigation into the impact of dissolution/precipitation mechanisms on CO_2 injectivity in the wellbore and far field regions. *Int. J. Greenhouse Gas Control* **2011**, *5* (3), 579−588.
(21) Zhang, L.; Soong, Y.; Dilmore, R.; Lopano, C. Numerical simulation of porosity and permeability evolution of Mount Simon sandstone under geological carbon sequestration conditions. *Chem. Geol.* **2015**, *403*, 1−12.
(22) Cao, P.; Karpyn, Z. T.; Li, L. Self-healing of cement fractures under dynamic flow of CO_2-rich brine. *Water Resour. Res.* **2015**, *51* (6), 4684−4701.
(23) Steefel, C.; Depaolo, D.; Lichtner, P. Reactive transport modeling: An essential tool and a new research approach for the Earth sciences. *Earth Planet. Sci. Lett.* **2005**, *240* (3−4), 539−558.
(24) Marini, L. Geological sequestration of carbon dioxide: Thermodynamics, kinetics, and reaction path modeling. In *Geological Sequestration of Carbon Dioxide: Thermodynamics, Kinetics, and Reaction Path Modeling*; Elsevier, 2007; Vol. *11*, pp 319−409.
(25) Schaef, H. T.; McGrail, B. P.; Owen, A. T. Carbonate mineralization of volcanic province basalts. *Int. J. Greenhouse Gas Control* **2010**, *4* (2), 249−261.
(26) Paukert, A. N.; Matter, J. M.; Kelemen, P. B.; Shock, E. L.; Havig, J. R. Reaction path modeling of enhanced in situ CO_2 mineralization for carbon sequestration in the peridotite of the Samail Ophiolite, Sultanate of Oman. *Chem. Geol.* **2012**, *330*−*331*, 86−100.
(27) Wang, F.; Giammar, D. E. Forsterite dissolution in saline water at elevated temperature and high CO_2 pressure. *Environ. Sci. Technol.* **2013**, *47* (1), 168−173.
(28) Rosenbauer, R. J.; Thomas, B.; Bischoff, J. L.; Palandri, J. Carbon sequestration via reaction with basaltic rocks: Geochemical modeling and experimental results. *Geochim. Cosmochim. Acta* **2012**, *89*, 116−133.
(29) King, H. E.; Plumper, O.; Putnis, A. Effect of secondary phase formation on the carbonation of olivine. *Environ. Sci. Technol.* **2010**, *44*, 6503−6509.
(30) Aradóttir, E. S. P.; Sonnenthal, E. L.; Björnsson, G.; Jónsson, H. Multidimensional reactive transport modeling of CO_2 mineral sequestration in basalts at the Hellisheidi geothermal field, Iceland. *Int. J. Greenhouse Gas Control* **2012**, *9*, 24−40.
(31) Steefel, C. I.; Appelo, C. A. J.; Arora, B.; Jacques, D.; Kalbacher, T.; Kolditz, O.; Lagneau, V.; Lichtner, P. C.; Mayer, K. U.; Meeussen, J. C. L.; et al. Reactive transport codes for subsurface environmental simulation. *Comput. Geosci.* **2015**, *19* (3), 445−478.
(32) Deng, H.; Molins, S.; Steefel, C.; DePaolo, D.; Voltolini, M.; Yang, L.; Ajo-Franklin, J. A 2.5D reactive transport model for fracture alteration simulation. *Environ. Sci. Technol.* **2016**, *50* (14), 7564−7571.
(33) Soler, J. M. Two-dimensional reactive transport modeling of the alteration of a fractured limestone by hyperalkaline solutions at Maqarin (Jordan). *Appl. Geochem.* **2016**, *66*, 162−173.
(34) Brunet, J.-P. L.; Li, L.; Karpyn, Z. T.; Huerta, N. J. Fracture opening or self-sealing: Critical residence time as a unifying parameter for cement−CO_2−brine interactions. *Int. J. Greenhouse Gas Control* **2016**, *47*, 25−37.
(35) Arvidson, R. S. The dolomite problem: Control of precipitation kinetics by temperature and saturation state. *Am. J. Sci.* **1999**, *299* (4), 257−288.
(36) Roberts, J. A.; Bennett, P. C.; González, L. A.; Macpherson, G. L.; Milliken, K. L. Microbial precipitation of dolomite in methanogenic groundwater. *Geology* **2004**, *32* (4), 277−280.
(37) Steefel, C. I.; Van Cappellen, P. A new kinetic approach to modeling water-rock interaction: The role of nucleation, precursors, and Ostwald ripening. *Geochim. Cosmochim. Acta* **1990**, *54* (10), 2657−2677.
(38) Adeoye, J. T.; Menefee, A. H.; Xiong, W.; Wells, R. K.; Skemer, P. A.; Giammar, D. E.; Ellis, B. R. Effect of transport limitations and fluid properties on reaction products in fractures of unaltered and serpentinized basalt exposed to high PCO2 fluids. *Int. J. Greenhouse Gas Control* **2017**, *63*, 310−320.
(39) Wells, R.; Giammar, D.; Skemer, P. *Sample library of natural and artificial basalts*; 2016; https://edx.netl.doe.gov/dataset/sample-library-of-natural-and-artificial-basalts/revision_resource/2bcdd2f4-70f0-4b1c-afe7-d1d563680e0c.
(40) Duan, Z.; Sun, R. An improved model calculating CO_2 solubility in pure water and aqueous NaCl solutions from 273 to 533 K and from 0 to 2000 bar. *Chem. Geol.* **2003**, *193*, 257−271.
(41) Cadogan, S. P.; Maitland, G. C.; Trusler, J. P. M. Diffusion coefficients of CO_2 and N_2 in water at temperatures between 298.15 and 423.15 K at pressures up to 45 MPa. *J. Chem. Eng. Data* **2014**, *59* (2), 519−525.
(42) Black, J. R.; Carroll, S. A.; Haese, R. R. Rates of mineral dissolution under CO_2 storage conditions. *Chem. Geol.* **2015**, *399*, 134−144.
(43) Fritz, B.; Clément, A.; Amal, Y.; Noguera, C. Simulation of the nucleation and growth of simple clay minerals in weathering processes: The NANOKIN code. *Geochim. Cosmochim. Acta* **2009**, *73* (5), 1340−1358.
(44) Palandri, J. L.; Kharaka, Y. K. *A Compilation of Rate Parameters of Water-Mineral Interaction Kinetics for Application to Geochemical Modeling*; DTIC Document, 2004.
(45) Knauss, K. G.; Johnson, J. W.; Steefel, C. I. Evaluation of the impact of CO_2, co-contaminant gas, aqueous fluid and reservoir rock interactions on the geologic sequestration of CO_2. *Chem. Geol.* **2005**, *217* (3−4), 339−350.
(46) Teir, S.; Revitzer, H.; Eloneva, S.; Fogelholm, C.-J.; Zevenhoven, R. Dissolution of natural serpentinite in mineral and organic acids. *Int. J. Miner. Process.* **2007**, *83* (1−2), 36−46.
(47) Orlando, A.; Borrini, D.; Marini, L. Dissolution and carbonation of a serpentinite: Inferences from acid attack and high P−T experiments performed in aqueous solutions at variable salinity. *Appl. Geochem.* **2011**, *26* (8), 1569−1583.
(48) Pokrovsky, O. S.; Golubev, S. V.; Schott, J. Dissolution kinetics of calcite, dolomite and magnesite at 25 °C and 0 to 50 atm pCO_2. *Chem. Geol.* **2005**, *217* (3−4), 239−255.
(49) Golubev, S. V.; Bénézeth, P.; Schott, J.; Dandurand, J. L.; Castillo, A. Siderite dissolution kinetics in acidic aqueous solutions from 25 to 100 °C and 0 to 50 atm pCO_2. *Chem. Geol.* **2009**, *265* (1−2), 13−19.
(50) Pokrovsky, O. S.; Schott, J. Surface chemistry and dissolution kinetics of divalent metal carbonates. *Environ. Sci. Technol.* **2002**, *36* (3), 426−432.

DOI: 10.1021/acs.est.7b00326
Environ. Sci. Technol. 2017, 51, 9352−9362

(51) Carroll, S. A.; McNab, W. W.; Dai, Z.; Torres, S. C. Reactivity of Mount Simon Sandstone and the Eau Claire Shale under CO_2 storage conditions. *Environ. Sci. Technol.* **2013**, *47* (1), 252−261.
(52) Tester, J. W.; Worley, W. G.; Robinson, B. A.; Grigsby, C. O.; Feerer, J. L. Correlating quartz dissolution kinetics in pure water from 25 to 625C. *Geochim. Cosmochim. Acta* **1994**, *58* (11), 2407−2420.
(53) Huertas, F. J.; Chou, L.; Wollast, R. Mechanism of kaolinite dissolution at room temperature and pressure Part II: Kinetic study. *Geochim. Cosmochim. Acta* **1999**, *63* (19), 3261−3275.
(54) Ellis, B. R.; Peters, C. A. 3D Mapping of calcite and a demonstration of its relevance to permeability evolution in reactive fractures. *Adv. Water Resour.* **2016**, *95*, 246−253.
(55) Van Pham, T. H. *CO_2 Storage−simulations for Forecasting the Behavior of Injection CO_2 in Geological formations*, 2013.
(56) Gysi, A. P.; Stefánsson, A. CO_2−water−basalt interaction. Numerical simulation of low temperature CO_2 sequestration into basalts. *Geochim. Cosmochim. Acta* **2011**, *75* (17), 4728−4751.
(57) Gysi, A. P.; Stefánsson, A. CO_2-water−basalt interaction. Low temperature experiments and implications for CO_2 sequestration into basalts. *Geochim. Cosmochim. Acta* **2012**, *81*, 129−152.
(58) Hellevang, H.; Haile, B. G.; Tetteh, A. Experimental study to better understand factors affecting the CO $_2$ mineral trapping potential of basalt: Experimental study to better understand factors affecting the CO $_2$ mineral. *Greenhouse Gases: Sci. Technol.* **2017**, *7* (1), 143−157.
(59) Xiong, W.; Wells, R. K.; Giammar, D. E. Carbon sequestration in olivine and basalt powder packed beds. *Environ. Sci. Technol.* **2017**, *51* (4), 2105−2112.
(60) Qiao, C.; Li, L.; Johns, R. T.; Xu, J. Compositional modeling of dissolution-induced injectivity alteration during CO_2 flooding in carbonate reservoirs. *SPE J.* **2016**, *21* (3), 0809−0826.
(61) Daval, D.; Sissmann, O.; Menguy, N.; Saldi, G. D.; Guyot, F.; Martinez, I.; Corvisier, J.; Garcia, B.; Machouk, I.; Knauss, K. G.; et al. Influence of amorphous silica layer formation on the dissolution rate of olivine at 90°C and elevated pCO_2. *Chem. Geol.* **2011**, *284* (1−2), 193−209.
(62) Saldi, G. D.; Jordan, G.; Schott, J.; Oelkers, E. H. Magnesite growth rates as a function of temperature and saturation state. *Geochim. Cosmochim. Acta* **2009**, *73* (19), 5646−5657.
(63) Jimenez-Lopez, C.; Romanek, C. S. Precipitation kinetics and carbon isotope partitioning of inorganic siderite at 25°C and 1 atm. *Geochim. Cosmochim. Acta* **2004**, *68* (3), 557−571.

■ NOTE ADDED AFTER ASAP PUBLICATION

This paper was published on the Web on August 2, 2017, with the incorrect artwork for Figure 1. The corrected version was reposted on August 3, 2017.

DOI: 10.1021/acs.est.7b00326
Environ. Sci. Technol. 2017, 51, 9352−9362